Kidney Stone Classification Using Multimodal Multiphoton Microscopy

Matthew Gleeson, Joséphine Morizet, Pierre Mahou, Michel Daudon, Dominique Bazin, Chiara Stringari, Marie-Claire Schanne-Klein, Emmanuel Beaurepaire

ACS Photonics

pubs.acs.org/journal/apchd5
Article

Kidney Stone Classification Using Multimodal Multiphoton Microscopy

Matthew Gleeson,*,‖ Joséphine Morizet,‖ Pierre Mahou, Michel Daudon, Dominique Bazin, Chiara Stringari, Marie-Claire Schanne-Klein,*,‖ and Emmanuel Beaurepaire*,‖

Cite This: ACS Photonics 2023, 10, 3594−3604
Read Online

ACCESS | Metrics & More | Article Recommendations | Supporting Information

ABSTRACT: Kidney stones are a common form of nephrolithiasis, affecting up to 15% of the world's population with a high probability of recurrence. These stones exhibit various chemical compositions and crystalline forms associated with different etiologies. Classification of the stones' components is necessary to optimize treatment and suggest lifestyle changes to reduce the risk of recurrence. Current characterization methods usually require extensive sample preparation or are too detailed for the needs of a high-throughput laboratory. In this article, we present a kidney stone component classification scheme based on the multiphoton response of crushed samples that is label-free, requires minimal sample amounts, and simple preparation. We measure two-photon excited fluorescence, which is sensitive to protein content, second-harmonic generation, which is sensitive to crystalline symmetry, and polarization-resolved third-harmonic generation (pTHG), which is sensitive to crystal heterogeneity and birefringence. The combination of these three contrast modes can distinguish different materials, specifically calcium oxalate in monohydrate (COM), dihydrate (COD), or amorphous forms, cystine, and carbonate apatite. In addition, pTHG images have the potential to distinguish between COM and COD fragments and to provide information on the submicron organization of carbonate apatite fragments.

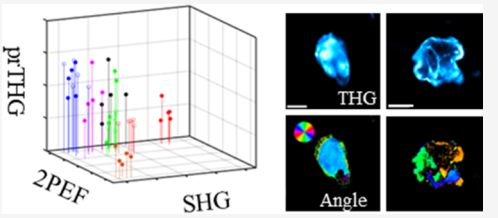

KEYWORDS: *nonlinear optics, polarized third-harmonic generation, calcium oxalate*

INTRODUCTION

Kidney stones (KS) are hard mineral deposits that form as a result of over-saturation of urine. After nucleation, growth, and subsequent aggregation, a large ensemble of aggregated crystalline material may be stabilized, resulting in the formation of a KS. A common initial cause of KS formation is related to alimentation disorder.[1] KS are commonplace, affecting 1.7−15% of the world's population at least once, with a 50% chance of recurrence within 5 years.[2] The high rate of recurrence can be due to a failure to correct the metabolic abnormalities responsible for its formation and may also be favored by the presence of residual fragments after urological treatment, acting as seeds for regrowth. Knowledge of the morphology and composition of a KS can be used to infer growth conditions,[1,3] as the final form reflects both the underlying pathology and the location within the urinary tract where the stone formed. The major component of a typical KS is calcium oxalate (CaC_2O_4) in the monohydrate (COM, whewellite) or dihydrate (COD, weddellite) form, which accounts for 60−70% of the urinary stone. Other common constituents are uric acid, struvite, carbonate apatite, brushite, and cystine.[3] Proteins can be incorporated and influence the stone structure.[4,5] A summary of the classification of stones according to their common causes is given in reference 6. In particular, COM KS are mainly associated with hyperoxaluria and COD KS with hypercalciuria; hence, knowledge of the composition of the stone is necessary to target the appropriate therapeutic treatment and provide the patient with recommendations for subsequent lifestyle changes.

Treatment options include ureteroscopy to remove the KS with a thin flexible ureteroscope. Fragmentation with a holmium laser[6] may allow for a natural passage of the stone fragments. Larger stones may require percutaneous nephrolithotomy in which the stone is extracted through keyhole surgery.[7] The most common treatment has been the use of extracorporeal shockwave lithotripsy, a noninvasive procedure that uses shockwaves to fragment the stone and allow it to pass naturally.[8] However, the optimal shockwave profile requires classification of the KS type based on its physiochemical composition.[1] Extracorporeal shockwave lithotripsy is now supplanted by flexible ureteroscopy using thulium lasers, which are more efficient for reducing stones into a powder easily evacuated in urine.[9]

KS are composed of multiple crystalline domains. Established methods for KS component characterization include optical microscopy,[1,10] Fourier transform IR spectroscopy,[1] Raman spectroscopy,[6,11−14] scanning electron microscopy

Received: May 16, 2023
Published: September 26, 2023

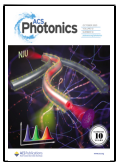

(SEM),[15] and X-ray crystallography.[16] FTIR spectroscopy is the reference method for KS routine analysis,[17,18] but it suffers from some limitations (complex sample preparation, possible interference with water, and overlapped peaks for some minerals). Alternatively, SEM equipped with an energy-dispersive X-ray spectrometer can provide detailed morphology and composition,[19] but requires a vacuum chamber, expert interpretation, and is too detailed for the needs of a high-throughput laboratory.[1] Similarly, accurate crystallographic information can be gathered with powder neutron diffraction[1] or X-ray crystallography,[16] but these methods are not compatible with rapid classification in a clinical setting. Overall, these techniques provide detailed information at the expense of sample preparation time or the need to maintain vacuum chambers. In this context, light microscopy at low magnification is a convenient method for fast etiological diagnosis in complement to FTIR or other physical methods.[6,20] Optical microscopy appears also to be ideally suited to fill the gap between the 10^{-5} m FTIR and 10^{-8} m SEM scales. In particular, multiphoton microscopy could prove useful for characterizing KS components, bypassing the need for pellet preparation or vacuum systems. Recent efforts using endogenous fluorescence have yielded promising results despite limited spectral information.[21] Alternatively, Raman spectroscopy has been used to successfully classify KS components,[11−13] albeit at the cost of long acquisition times.[22] Some studies have suggested that this difficulty may be circumvented by using coherent anti-stokes Raman scattering (CARS) microscopy to correlate chemical information with morphology.[23]

In this paper, we present a novel classification scheme for kidney stones based on combined multiphoton fluorescence/harmonic responses of powdered samples and demonstrate its suitability for distinguishing between several types of KS. Our scheme requires only a small amount of powder with no further preparation, is label-free, performed under ambient conditions with short acquisition times, and is easy to interpret. It is based on the detection of two-photon excited fluorescence (2PEF), second-harmonic generation (SHG), and polarization-resolved third-harmonic generation (pTHG) signals from KS fragments. Third-harmonic generation (THG) is used to detect stone fragments; 2PEF serves as an indicator of protein content; SHG indicates whether the KS fragment is non-centrosymmetric; pTHG detects birefringence.[24] We show that KS and control samples with different compositions exhibit different combinations of multiphoton responses.

MATERIALS AND METHODS

Samples. An ethical committee was not required for this observational study according to Helsinki law and the French Institutional Committee. Patients were informed at the time the KS were sampled that kidney tissue could be used for scientific purpose and consented to this study. We analyzed one synthetic sample of amorphous calcium oxalate (ACO)[25] to serve as a negative control sample with no SHG, fluorescence, or birefringence. We then analyzed two COM samples with an unknown protein content, three COD samples, two of which were 99% COD 1% protein and the other was 96% COD 4% protein, two samples of cystine with a protein content of 1−3%,[26] and finally one carbonate apatite sample with 4% protein content. All of the samples along with their chemical composition, crystalline structure, and protein content are listed in Table S1. KS were selected based on the purity of their physiochemical composition rather than the patient's condition.

The KS are crushed into a fine powder, shown in Figure 1a. The powdered KS are placed on a 170-μm-thick glass

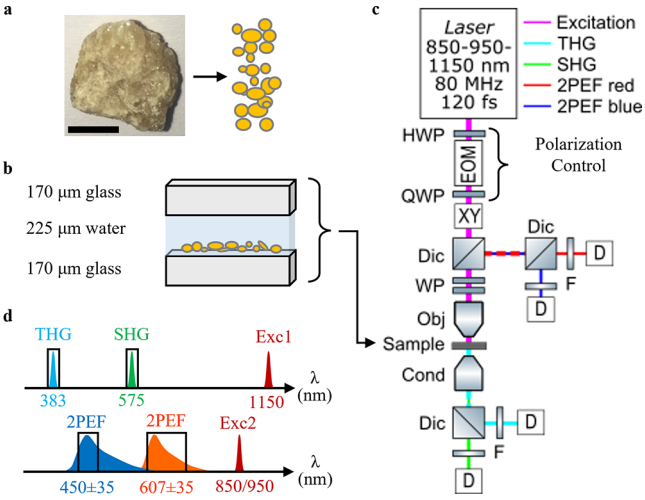

Figure 1. Experimental setup. (a) Illustration of minimal sample preparation, consisting in crushing the kidney stone into microfragments. Scale bar is 2 mm. (b) Sample chamber consisting of 170 μm glass coverslips 225 μm apart with fragments suspended in water. (c) Schematic of microscope. HWP: half wave plate; EOM: electrooptic modulator for polarization control; QWP: quarter wave plate; XY: beam scanning; Dic: dichroic mirror; WP: wave plates; Obj: objective; Cond: condenser; F: filter; D: detector. (d) Multiphoton signals measured.

coverslip. Adding an O-ring spacer 225-μm-thick allows for water to be added. Another 170 μm coverslip is placed on top. Construction is shown in Figure 1b. The weight of the sample required was likely in the milligram range, though only a fraction of that was imaged during experiments.

Experimental Setup. Images are recorded with a custom multiphoton microscope, shown in Figure 1c. The linearly polarized laser beam (80 MHz, 110 fs, tunable from 690 to 1300 nm, Insight X3, SpectraPhysics) is scanned by galvanometric mirrors (Cambridge Technology). It is focused by a water immersion objective (25×, 1.05 NA, Olympus) with 50 mW incident power on the sample and pixel dwell time of 5 μs. Pixel size is set to 0.25 μm for pTHG images and 0.5 μm for 2PEF and THG/SHG images. The axial step for Z scans is 0.3 μm. Signals recorded are shown in Figure 1d. THG/SHG is excited at 1100 nm (ACO and COM samples) or 1150 nm (remaining samples). THG/SHG are collected in transmission by a condenser lens (Olympus). Excitation light is filtered out by a 705 nm short pass filter (Semrock Brightline multiphoton, FF705-DiO1), and then the signal is split with a 495 nm dichroic filter (Semrock Brightline FF495-DiO3) to detect SHG using a 575/19 nm band pass filter (Semrock Brightline Fluorescence FF01-575/19-25) and THG using a 390/40 nm band pass filter (Semrock Brightline Fluorescence FF01-390/40-25). 2PEF is excited at 850 or 950 nm and collected using the epidetection mode. The excitation beam is filtered out by a 680 nm short pass filter (Semrock Brightline multiphoton FF01-680/SP-25) and the signal is split with a 495 nm dichroic filter (Semrock Brightline FF495-DiO3). Blue wavelengths are detected using a 450/70 nm band pass filter (Semrock Brightline Fluorescence FF01-450/70-25) and the red channel

https://doi.org/10.1021/acsphotonics.3c00651
ACS Photonics 2023, 10, 3594−3604

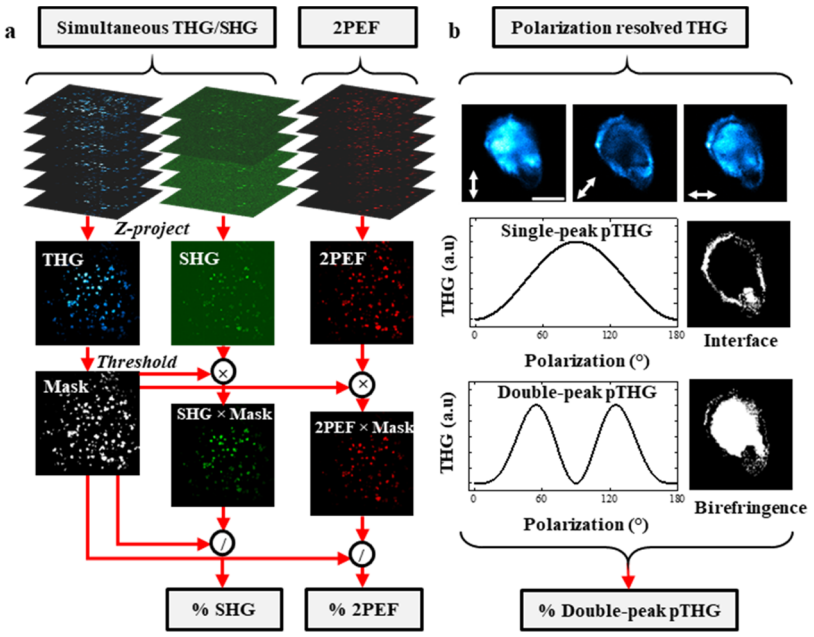

Figure 2. Analysis of multimodal multiphoton data: extraction of SHG, 2PEF, and single-peak vs double-peak pTHG scores. (a) Correlative THG, SHG, and 2PEF Z-stacks are Z-projected. KS particles are detected using the THG projection image, resulting in a particle binary mask. This mask is then used to measure the fraction of SHG-positive pixels and 2PEF-positive pixels among all of the THG-positive pixels. The field of view is 735 μm^2 in all images of panel (a). (b) Example of zoomed-in pTHG images from an individual fragment, with the arrow indicating the polarization direction of laser excitation. Fourier-based analysis[24] classifies pixels as either being single-peak, double-peak, or a more complex response. This classification is applied to 50 particles per sample and is used to assess the fraction of THG-positive pixels originating from particle birefringence ("double-peak pTHG"). Scale bar is 10 μm in panel (b).

2PEF is filtered by a 607/70 nm band pass filter (Semrock Brightline FF01-607/70-25). To compensate for the difference in focus between THG/SHG and 2PEF image stacks due to chromatic issues, the stage is moved by 1 μm (950 nm) or 2 μm (850 nm) to ensure the same volume is imaged. THG and red 2PEF signal are recorded and quantified by photon counting PMTs (P25PC, SensTech). SHG and blue 2PEF are recorded with GaAsP detectors (H7422P-40, Hamamatsu).

The THG polarization response is obtained by recording a series of images excited by linear polarizations rotated from 0 to 170° in 10° increments. The laser polarization is controlled by an electrooptic modulator set between two wave plates (350-160-02, Conoptics). Ellipticity is minimized by a pair of half and quarter wave plates prior to the objective, giving an ellipticity of 1.5% at 1150 nm at the sample plane. For pTHG analysis, fragments are imaged individually. Image acquisition and microscope control are done with in-house-developed LabVIEW software.

Multimodal Multiphoton Classification. The image acquisition process and classification scheme are detailed in Figure 2. First, Z-stacks are recorded to measure THG/SHG simultaneously or 2PEF; see Figure 2a. Each of the recorded Z-stacks are summed up and normalized to the number of images in each stack. As THG occurs regardless of the crystal structure or the presence of proteins, every KS fragment within the field of view is detected. The THG image is thus processed in MATLAB to remove the background and generate a binary mask. Objects with a connectivity of less than 8 pixels or a mean THG value less than a preset threshold *Thr* are discarded. Then, the resulting binary mask is applied to the SHG and 2PEF images. Finally, the mean signal within the fragment's boundaries and the probability of each signal are measured. The probability of each signal (2PEF, SHG, double-peak pTHG) is defined as the fraction of pixels with nonzero values (*i.e.*, greater than *Thr*) for each signal within the detected fragments. The identification of double-peak (or "birefringence") THG pixels (Figure 2b) is done on a reduced number of fragments using pTHG acquisitions as discussed below.

Average acquisition time for a Z-stack (800 × 800 pixels, average of 38 frames, pixel dwell time of 5 μs) was approximately 2 min, not including the flyback time of the galvo scanners between lines. Each sample measured five fields of view, scanned with three different wavelengths, for a total acquisition time of around 30 min. Computation time for the Z-stacks per sample data takes approximately 35 s. The PC used was an i7-10700T 2 GHz Intel processor with 32 GB RAM.

pTHG Theory. As discussed in previous studies of THG microscopy, no THG is obtained from within a homogeneous isotropic medium due to the phase mismatch associated with the Gouy phase shift of the excitation beam.[27−29] THG can be observed either near interfaces[28] or in the volume of birefringent materials.[30−32] These two types of signals result from different phase-matching mechanisms and can generally be distinguished by their dependence on the incident polarization.[24] However, a general analytical description of pTHG from an anisotropic and heterogeneous sample is complex. Indeed, several experimental parameters can alter THG intensity in a polarization-dependent manner, most importantly the materials' anisotropy[30−33] and sub-wavelength field distortions near index discontinuities.[34,35] We assume here that the material has hexagonal symmetry as in previous studies,[24,31,32] which reduces the THG response to only three independent $\chi^{(3)}$ tensor components $\{\chi_{\parallel}^{(3)}, \chi_{cr}^{(3)}, \chi_{\perp}^{(3)}\}$.[27] Furthermore, we assume that its principal axis lies within the

https://doi.org/10.1021/acsphotonics.3c00651
ACS Photonics 2023, 10, 3594−3604

imaging plane (Figure S1). This simplified model is analytically tractable and provides an overview of the three main situations encountered in pTHG imaging, namely, when the excitation beam is focused (i) at the surface of an anisotropic material, (ii) inside a birefringent material, and (iii) near an index-mismatched interface parallel to the beam propagation direction. We here recall the main equations, and additional formal descriptions are provided as supporting information; see Section S2.

(i) When the beam is focused at the surface of an anisotropic material, assuming the surface is perpendicular to the beam propagation direction and neglecting polarization-dependent field distortions, the pTHG response can be written in the general form

$$\begin{aligned}\mathrm{THG_H}(\phi) &\propto (|\chi_{\parallel}^{(3)}\cos^3(\phi-\phi_0) + \chi_{cr}^{(3)}\cos(\phi-\phi_0)\sin^2(\phi-\phi_0)|^2 \\ &\quad + |\chi_{\parallel}^{(3)}\cos^2(\phi-\phi_0)\sin(\phi-\phi_0) + \chi_{\perp}^{(3)}\sin^3(\phi-\phi_0)|^2)\, I^3 \end{aligned} \tag{1}$$

where I is the excitation intensity, ϕ is the angle of the incident polarization in the imaging plane, and ϕ_0 is the angle of the crystal axis in the imaging plane (Figures S1 and S2). This response can exhibit various profiles depending on the ratios between the three independent $\chi^{(3)}$ tensor elements. It exhibits a single maximum over the [0−180°] range if the $\chi_{\parallel}^{(3)}$ term is dominant; but two maxima can be observed if $\chi_{\parallel}^{(3)}$ and $\chi_{\perp}^{(3)}$ have comparable magnitudes, as was confirmed experimentally in the case of X-oriented calcite.[30] Orientation of the materials' axes with respect to the imaging plane, crystalline symmetry, and field distortion due to index heterogeneity can also alter the pTHG response.

(ii) In the case of birefringence THG, *i.e.*, when THG is obtained from the bulk of an anisotropic material possessing a birefringence large enough to compensate the phase mismatch due to the Gouy phase shift, the THG intensity can be expressed in the simplified form[24,32]

$$\mathrm{THG_{biref}}(\phi) \propto \cos^4(\phi-\phi_0)\sin^2(\phi-\phi_0)|\chi_{cr}^{(3)}|^2 I^3$$

in the case of positive birefringence (2a)

$$\mathrm{THG_{biref}}(\phi) \propto \cos^2(\phi-\phi_0)\sin^4(\phi-\phi_0)|\chi_{cr}^{(3)}|^2 I^3$$

in the case of negative birefringence (2b)

with the same notations as in case (i). This expression corresponds to a characteristic double-peaked profile as shown in Figure 2b.

(iii) In the case of pTHG from an interface parallel to the beam propagation, *i.e.*, when a linearly polarized excitation beam is focused near a vertical discontinuity of the refractive index, the THG process is significantly altered by field distortions[34,35] and cannot be easily described analytically. In high-NA microscopy experiments, the signal is often found to follow a polarization dependence in the form[33]

$$\mathrm{THG_V}(\phi) \propto A + B\cos^2(\phi-\phi_0) I^3 \tag{3}$$

where A and B are constants. This expression corresponds to a single-peaked curve as shown in Figure 2b.

Therefore, in the general case, the pTHG response of an anisotropic sample can exhibit different profiles, which depend in a complex way on the ratios between the $\chi^{(3)}$ tensor elements, the crystalline orientation with respect to the imaging plane, the localization of the beam focus with respect to interfaces, and index discontinuities in the sample. However, from a practical point of view, the detection of various orders in the Fourier transform of the pTHG response provides an efficient means to distinguish between simple cases such as (vertical) interface THG and birefringence THG.[24]

pTHG Data Processing. After recording a series of THG images with excitation polarization angles ranging from 0 to 170° in 10° increments, the processing is split into the following steps. First, the pTHG profile is normalized to that of a horizontal interface to account for the slight differences in excitation power according to the excitation polarization orientation. Second, the modulus a_u and the angle $\phi_{0,u}$ of the Fourier coefficients $a_u \exp[u \times i(\phi-\phi_{0,u})]$ are calculated for each pixel from the fast Fourier transform (FFT) of the pTHG intensity stack. Third, this data is used to determine which pixels exhibit a predominantly "single-peak" or "double-peak" pTHG response. Double-peak pTHG is often a signature of birefringence (eqs 2a, 2b) and is characterized by significant Fourier components up to order 6. Single-peak pTHG is often a signature of interface THG (eq 3) and is characterized by significant Fourier components up to order 2 only. Fourier components at order 4 and 6 are thus specific of double-peak responses. We therefore calculated coefficients of determination R^2 for every pixel between the experimental pTHG response and the "double-peak" component $I_{2\mathrm{peak}}^{\mathrm{FFT}}(\phi)$ reconstructed from the Fourier coefficients a_0, a_4, and a_6 (eq 4) or the single-peak one $I_{1\mathrm{peak}}^{\mathrm{FFT}}(\phi)$ reconstructed from the Fourier coefficients a_0 and a_2 (eq 5)

$$I_{2\mathrm{peak}}^{\mathrm{FFT}}(\phi) \propto a_0 + a_4\cos[4(\phi-\phi_{0,4})] + a_6\cos[6(\phi-\phi_{0,6})] \tag{4}$$

$$I_{1\mathrm{peak}}^{\mathrm{FFT}}(\phi) \propto a_0 + a_2\cos[2(\phi-\phi_{0,2})] \tag{5}$$

Fourth, these R^2 maps serve to build masks corresponding to double-peak or single-peak responses using $R^2 = 0.5$ as a threshold. The resulting images also map the angle $\phi_{0,2}$, which provides indications on sample heterogeneity and orientation. Note that the angle $\phi_{0,2}$ is mapped both for single-peak and double-peak responses since the Fourier component at order 2 is common to both responses, although eq 4 only uses components at orders 2 and 4 for a better separation of the two types of responses. Voxels not classified as clearly "single-peak" or "double-peak" correspond to complex situations such as several domains contributing to a single pixel, nonhexagonal symmetries, or anisotropic sample regions with main axis tilted out of the imaging plane.

The typical pTHG imaging time per fragment was a few seconds. The computation time for each sample containing 50 fragments was about 1 min.

RESULTS AND DISCUSSION

For each sample, we recorded THG/SHG and 2PEF image stacks of five large fields of view (FOV, Ø735 μm), containing

https://doi.org/10.1021/acsphotonics.3c00651
ACS Photonics 2023, 10, 3594−3604

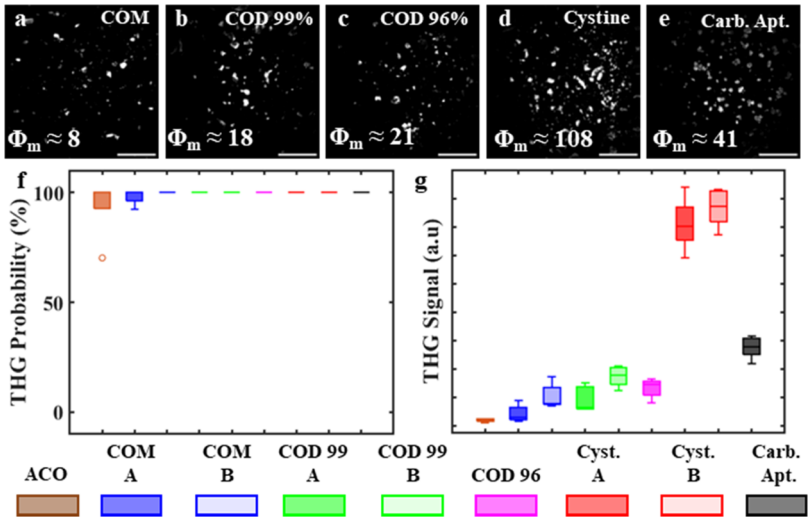

Figure 3. THG response of several kidney stones and control sample. (a) COM, (b) COD 99%, (c) COD 96%, (d) cystine, and (e) carbonate apatite samples. Image contrast has been stretched for the sake of clarity. Scale bars are 200 μm. Inset Φ_m refers to mean number of photons from detected fragments for each sample type. Box plots for THG: (f) probability and (g) signal.

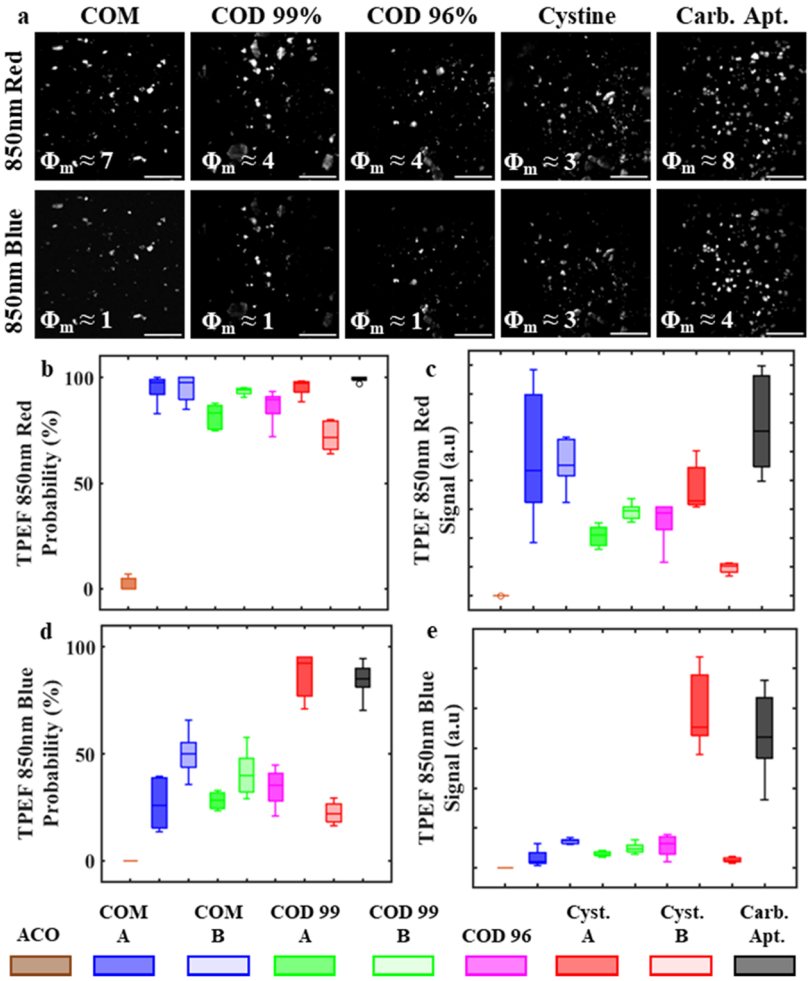

Figure 4. 2PEF response, excited at 850 nm, of several kidney stones and control sample. (a) Representative 2PEF images for COM, COD 99%, COD 96%, cystine, and carbonate apatite samples. First row, red fluorescence excited at 850 nm; second row, blue fluorescence excited at 850 nm. Inset Φ_m refers to mean number of photons in the detected fragments for each sample type. Image contrast has been stretched for the sake of clarity. Scale bars are 200 μm. (b) Probability and (c) signal levels of red channel fluorescence excited at 850 nm. (d) Probability and (e) signal levels of blue fluorescence excited at 850 nm.

https://doi.org/10.1021/acsphotonics.3c00651
ACS Photonics 2023, 10, 3594−3604

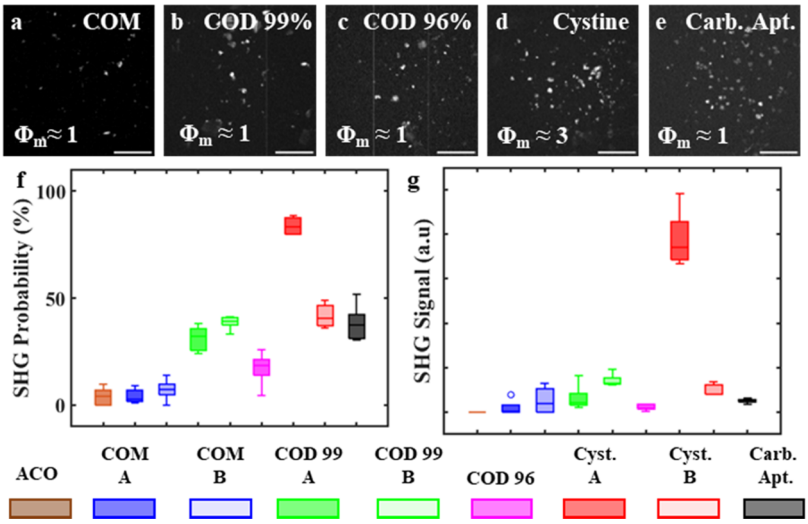

Figure 5. SHG response of several kidney stones and control sample. (a) COM, (b) COD 99%, (c) COD 96%, (d) cystine, and (e) carbonate apatite samples. Inset Φ_m refers to mean number of photons in the detected fragments for each sample type. Image contrast has been stretched for the sake of clarity. Scale bars are 200 μm. Box plots for SHG: (f) probability and (g) signal.

200−2000 powder fragments across the five FOV for each KS sample (Figures 3−5 and S1). We then performed 2D pTHG analyses of 10 fragments in a smaller region of the same FOV, which resulted in 50 pTHG analyses per sample (Figure 6). For each acquisition, THG image projections were first used to detect fragments via signal thresholding. The resulting binary masks were used for the quantitative analyses of all signals (Figure 2). In the following paragraphs, we discuss the observed statistics for THG, SHG, and 2PEF and finally combined pTHG-SHG-2PEF measurements.

Representative THG images for all sample types are shown in Figure 3a−e. They illustrate that THG recorded with a single polarization state efficiently highlights particles with a variety of sizes and shapes over the FOV. For each sample, the proportions of THG-positive pixels (see Materials and Methods) within the detected fragments are presented as box plots in Figure 3f and the distribution of measured THG signals is shown in Figure 3g. The fraction of THG-positive pixels within detected fragments is close to 100% for all sample types, which is expected since the analysis is performed on Z-projected images encompassing the fragments' inner domains and outer interfaces. The THG signal, Figure 3g, shows a more varied response. ACO has the lowest amount of THG, as expected due to its amorphous nature that results in isotropic bulk fragments, which prevents any THG due to birefringence. Both COM and COD exhibit intersample variability. Of note, the cystine and carbonate apatite samples generated significantly more THG relative to COM and COD. Overall, the measurements indicate that THG is useful for particle detection but is of limited use as an identification metric outside of separating amorphous from crystalline material and distinguishing cystine based on its high THG signal.

Representative images of blue and red fluorescence excited at 850 nm are shown in Figure 4a, with box plots showing the probability in Figure 4b,d and signal in Figure 4c,e. We remind that the 2PEF probability is the proportion of pixels that produce significant 2PEF within the fragments detected using THG. Complementary data on the red-emitted 2PEF upon 950 nm excitation is presented in Figure S2.

The ACO sample fragments exhibit low 2PEF probability and signal. This is expected given that ACO is a synthetic sample with no protein content. In contrast, most fragments of both COM samples exhibit fluorescence, as indicated by the similarity between the THG images (Figure 3a) and 2PEF images (Figure 4a). Although the exact amount of proteins in COM samples is unknown, they do contain proteins due to the absorption and integration of proteins onto the surface of the stone.[1] As we test a random selection of microfragments, we cannot know from where in the complete stone the fragments have come; hence, random spikes of high fluorescence on some particles may indicate they originate from the surface of the stone where proteins aggregate. The 2PEF response of COD 99% and COD 96% shows similar probabilities of generating 2PEF and slightly lower signal levels, despite COD 96% having four times more proteins. We measured that red 2PEF from COD is slightly lower than red 2PEF from COM, in contrast with a previous study reporting a more pronounced difference.[21] 2PEF is observed in both cystine samples but cystine A exhibits higher 2PEF probability and signal than cystine B. The difference is more pronounced in the blue channel, suggesting that the fluorescence profile can vary between KS. The amount of proteins contained in the cystine samples is presumably between 1 and 3% (similar to a typical KS protein content), but the exact quantity is unknown because it cannot be measured using IR spectroscopy due to the intense absorption of cystine in the same spectroscopic region as the proteins. The large intersample variability of 2PEF in cystine samples may reflect the diversity of response in KS. Carbonate apatite shows the highest 2PEF probability and signal of all samples tested, due to its high protein content. Of note, we find that carbonate apatite fragments specifically exhibit a consistently high probability and mean signal of red fluorescence compared to all of the crystal types analyzed in our study. The probability and signal level of blue 2PEF is similar to that of cystine A. This observation of strong fluorescence in carbonate apatite is consistent with a previous report comparing fluorescence levels in carbonate apatite and COM.[23] To add a dimension to better distinguish the samples, we will now examine their SHG responses.

Representative SHG images are presented in Figure 5a−e along with statistics of the SHG probability shown in Figure 5f and signal level in Figure 5g. The ACO sample, which serves as

https://doi.org/10.1021/acsphotonics.3c00651
ACS Photonics 2023, 10, 3594−3604

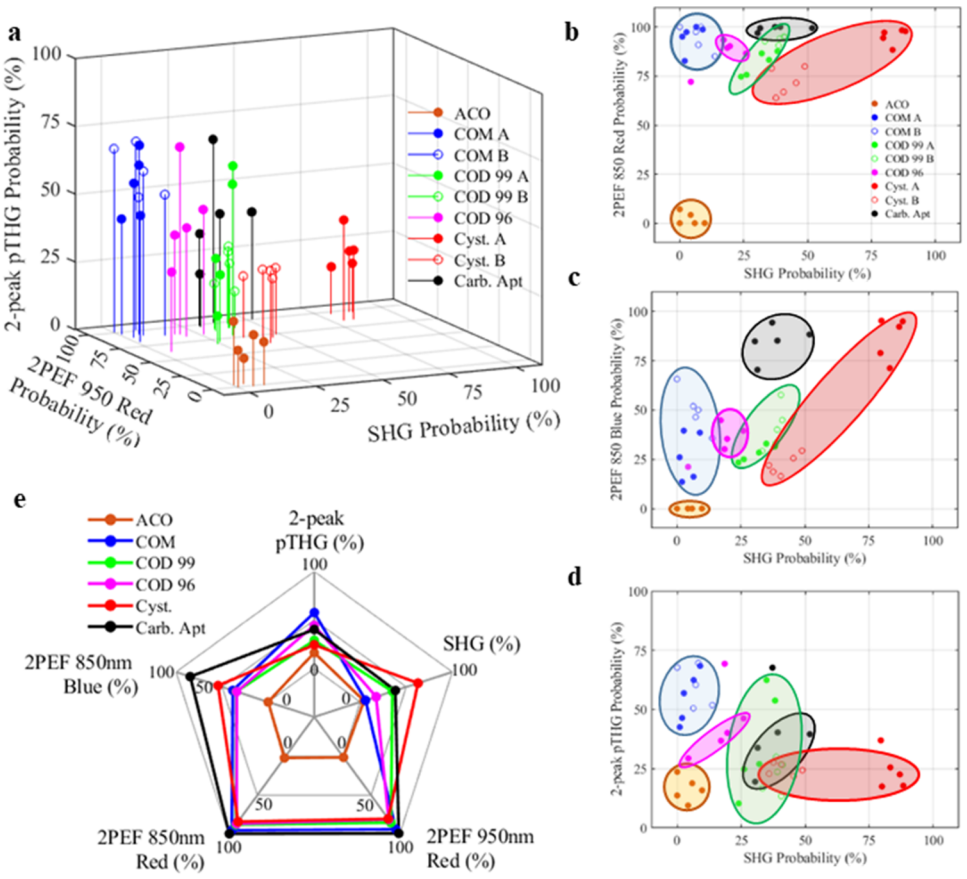

Figure 6. Classification of kidney stones and control sample using their multimodal pTHG-SHG-2PEF signatures. (a–d) Distribution of KS and control samples in the parametric space based on the probability of double-peak pTHG, SHG, and red/blue 2PEF excited at 850/950 nm. (a) 3D representation using red channel 2PEF excited at 950 nm. (b) Projection in the SHG-red 2PEF 850 nm plane. Ellipses are a guide for the eye. (c) Similar representation using blue 2PEF 850 nm and SHG. (d) Projection in the SHG-pTHG plane. (e) Spider plot with each sample response averaged out to a single point.

our negative control, exhibits low SHG probability and even lower SHG signal, as expected, because of its amorphous structure. Similarly, both COM samples exhibit low SHG probability (<10%) and signal, indicating that they are mostly made of centrosymmetric crystalline fragments or amorphous ones.[23] This is in good agreement with the centrosymmetric nature of COM crystals. In rare cases, strong SHG was detected from a few fragment subdomains, which can be interpreted as a signature of a locally non-centrosymmetric structure. This may be related to the high protein content as shown by the 2PEF data. Both COD 99% (Figure 5b) and COD 96% (Figure 5c) samples appear to exhibit more SHG active fragments than the COM samples, while they are also expected to exhibit a centrosymmetric crystalline structure. COD 99% samples exhibit slightly higher SHG probability and signal than the COD 96% sample. SHG efficiency from COD samples is here anticorrelated with the protein content, which changes from 1 to 4% for COD 96%. Cystine is a common hexagonal non-centrosymmetric KS component related to a genetic disorder.[36,37] Accordingly, a widespread match between the THG (Figure 3d) and SHG (Figure 5d) images is observed, which shows that most fragments are non-centrosymmetric. However, there is a significant variability in terms of SHG probability and signal between the two cystine samples examined in our study. At a macroscale inspection, cystine B had a more glass-like look and was much more fragile compared to cystine A. Photos are shown in Figure S3. This is in good agreement with our SHG data and previous reports.[38] Carbonate apatite is also non-centrosymmetric and accordingly exhibits a clear overlap of fragments detected between the THG image (Figure 3e) and SHG image (Figure 5e). Its hexagonal symmetry is the same type as for cystine, and it exhibits a similar SHG probability, although the signal is low. Overall, these observations indicate that the SHG probability, which can be measured simultaneously with THG, is a useful metric for distinguishing between COM, COD, cystine, and carbonate apatite samples based on their crystalline content.

We now discuss the single-peak versus double-peak pTHG analysis and its combination with SHG and 2PEF probabilities. Data points in Figure 6 represent the average probability in each of the five FOV analyzed in every sample. Note that pTHG analyses are performed on a total of 50 fragments per sample, which is smaller than the number of fragments used for SHG or 2PEF analyses (typically 200–2000). Accordingly, double-peak pTHG probability generally exhibits a larger spread than SHG and 2PEF scores (Figure 6a,d). This variability may also reflect the variety of crystalline domains and orientations present in full KS. Given that KS grow over the course of several years, the characteristics of the KS can vary between the stone core interior and exterior, as previous imaging studies have found.[13,21,23]

As shown in Figure 6d, ACO displays a very low double-peak pTHG probability, which is consistent with its non-birefringent amorphous structure. The single-peak pTHG

https://doi.org/10.1021/acsphotonics.3c00651
ACS Photonics 2023, 10, 3594–3604

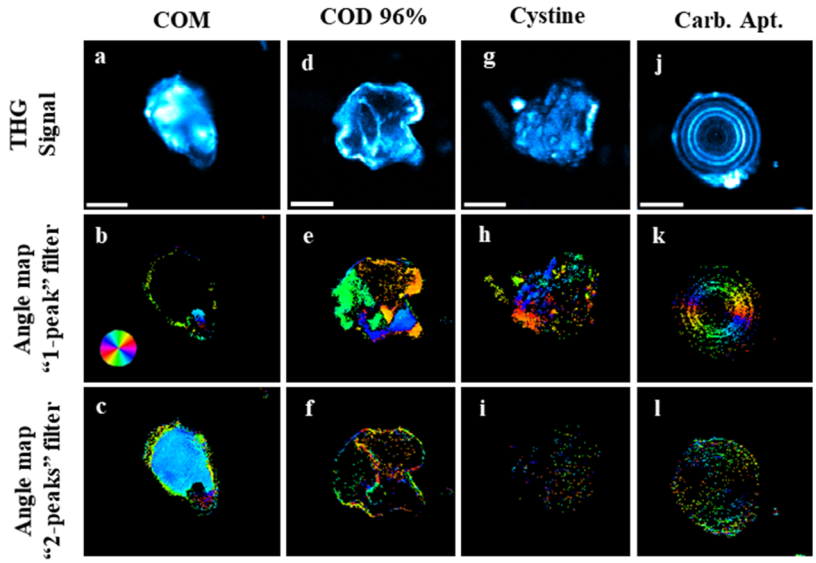

Figure 7. pTHG properties of representative kidney stones fragments. The first row shows the average THG signal. The second row shows pixels exhibiting a single-peaked pTHG response along with the angle $\phi_{0,2}$ coded according to the color when in the inset. The third row shows pixels exhibiting a double-peaked pTHG response along with the angle $\phi_{0,2}$. (a–c) COM, (d–f) COD 96%, (g–i) cystine, and (j–l) carbonate apatite. Scale bar is 10 μm in all images.

response exhibited by most pixels is thus indicative of interface THG, as expected. In contrast, fragments from both COM samples display the highest degree of double-peak pTHG pixels, namely, in the 40–70% range. This observation is indicative of a birefringent material, consistent with the fact that COM has previously been shown to be a positive biaxial crystal.[39] The probability of double-peak pTHG for the COD samples is lower than that of COM, namely, 25–50% for COD 96% excluding outliers and 10–60% for COD 99%. We observe that COD mainly exhibits single-peak pTHG as most points fall below 50% probability of being a double-peak response. The pTHG responses of cystine and carbonate apatite samples are also dominated by single-peak modulation. Cystine fragments exhibit a low and uniform range of double-peak pTHG probability, varying from 15 to 30%, uncorrelated with SHG probability. Carbonate apatite samples show a similar double-peak pTHG probability as COD 96%.

The combination of pTHG, SHG, and 2PEF probabilities into a single parametric plot is shown in Figure 6a–d. The 3D view presented in Figure 6a illustrates that the different KS components can be distinguished by their combined pTHG/SHG/2PEF responses. Taking the projection of the SHG-red 2PEF excited at 850 nm plane, Figure 6b, 2PEF easily distinguishes the synthetic ACO without any organic content from the KS with protein content. Carbonate apatite can also be distinguished using its strong, blue-shifted fluorescence component, Figure 6c. SHG probability is a particularly interesting signature for separating different KS types. Looking at the *x*-axis in Figure 6b–d, there is a clear separation between samples based on the material fragments probability of being non-centrosymmetric. An exception is separating ACO from the response of COM, as both are centrosymmetric, but this distinction is obtained by the double-peak THG probability as shown in Figure 6d. Similarly, despite the overlap of pTHG/SHG for COD 99% and carbonate apatite, the difference in blue 2PEF can be used to distinguish them instead. Altogether, the combination of the three metrics appears as an effective way to distinguish the different types of KS samples considered in the study. To improve discrimination, particularly for a KS that contains multiple materials, a principle component analysis enhanced by machine learning, similar to that applied in Raman spectroscopy,[12,40] could be beneficial.

A complementary way of displaying the multimodal multiphoton response of the KS sample is to use a spider plot including additional 2PEF dimensions, Figure 6e. To simplify the display, we average out the response between similar types of samples such that we get a single point to represent the double-peak pTHG/SHG/2PEF probabilities for each type of sample tested. Averaging out the probability of double-peak pTHG to a single point per sample type more clearly illustrates the difference between sample types. COM and COD 96% show the higher double-peak pTHG probability, while COD 99% is between that of cystine and carbonate apatite. SHG shows the difference between samples most clearly, with each KS type occupying a distinct position with the exception of COM and ACO, as previously discussed. The 2PEF responses on the spider plot show that given the general similarity of the fluorescence profile between material types, classification based on fluorescence alone, with the exception of blue channel 2PEF from carbonate apatite, is too coarse to distinguish all sample types, even when considering different 2PEF channels.

In summary, the parametric and spider plots presented in Figure 6 show that common KS component types can be distinguished from each other based on their multimodal multiphoton response. Notably, it includes COM and COD that are the most common KS and do not correspond to the same etiology. Remarkably, this method is applicable to micrometer-sized KS fragments, whose structural characterization is challenging using FTIR. Indeed, FTIR devices display a diffraction-limited spatial resolution of around 10 μm at 1000 cm^{-1}, which results in a poor signal-to-noise ratio in smaller fragments. Improvement of FTIR spatial resolution by means of attenuated total reflectance spectroscopy is quite low, while emerging high-resolution IR spectroscopies such as OPTIR (optical photothermal infrared) or AFM-IR (atomic force

https://doi.org/10.1021/acsphotonics.3c00651
ACS Photonics 2023, 10, 3594–3604

microscopy combined with IR spectroscopy) require a specific preparation of KS samples, which may be quite challenging.[41] In contrast, multimodal multiphoton characterization should be applicable to any micrometer-sized KS fragment, either *in vitro* or *in situ* within a biopsy.

Although the microscope used here was designed for academic research, it could be optimized for use in a clinical setting, but that is outside the scope of this study. Potential simplifications could be the use of fixed-wavelength laser sources, using a single wavelength for simultaneous 2PEF/SHG to remove the need to account for chromatic effects or replacing the EOM and galvanometric scan optics, which introduce significant beam ellipticity that must be corrected using additional wave plates, with a motorized half wave plate and piezoelectric stage. Alternatively, a standard widefield microscope could identify fragment locations before switching to multiphoton imaging of those fragments, or a microfluidic-based microscope with all signal detection in transmission and single axis laser scanning could have high throughput.

Finally, and as a perspective, we present pTHG maps of individual KS fragments in Figure 7 in order to discuss the origin of the pTHG response. The THG images presented along the top row show the variety in sample morphology. COM (Figure 7a–c) shows a smooth crystal fragment with single-peak pTHG along the fragment edge, as expected for a vertical interface, and a double-peak pTHG in the interior, as expected for birefringent bulk pTHG. Remarkably, the pTHG angle is uniform within the fragment, indicating that it is a monocrystal. This differs from the pTHG response of the COD fragment (Figure 7d–f) where the pTHG shows mainly single-peak responses, meaning that the contribution of birefringence to THG is negligible. Moreover, the single-peak pTHG angle map reveals several homogeneous regions with distinct orientations. This pattern may be attributed to the presence of several adjacent monocrystalline subdomains, which individually exhibit single-peak pTHG responses due to specific values of their THG tensor components. The cystine example in Figure 7g–i shows a fragment with multiple small domains, which exhibit predominantly single-peak pTHG. This pattern is consistent with vertical interface THG between micrometer-sized crystalline fragments. Interestingly, the carbonate apatite sample (Figure 7j–l) shows a pattern of radial density, highlighted as concentric rings in the THG image of Figure 7j. The pTHG response shows predominantly single-peak modulation, which indicates that the sample is composed of concentric crystalline subdomains that form vertical interfaces for THG imaging. The pTHG angle distribution is radial, consistent with the presence of concentric index-mismatched vertical interfaces.[34] Such a concentric structure is in line with a pathogenesis process of the calcification that has been described in different organs including kidney,[42] skin,[43] or breast[44] and attributes these micrometer spherical entities made of calcium phosphate apatite to the agglomeration of nanospherules. However, these spherical entities may display various kinds of internal structures, namely, homogeneous, concentric, and/or radial ones, as shown by SEM observations.[42−45] This diversity underlines the existence of very different pathogenesis growing processes and thus may be related to different diseases. Accordingly, precise characterization of these spherical structures may lead to the developments of new diagnostic tools of relevance for asymptomatic patients with urinary tract infection.[42,45] pTHG can probe the internal structure of these objects without preparation, potentially offering an opportunity for the development of new medical diagnosis tools. Recent advances in artificial intelligence-based image segmentation[46,47] may then be used to characterize the distribution of crystalline domains within fragments as another metric of classification.

CONCLUSIONS

In this work, we presented a novel multiphoton classification technique to distinguish common KS types based on the likelihood of KS fragments to generate specific combinations of 2PEF, SHG, and double-peak pTHG signals. We find that a combination of these different signals provides more discriminatory power than using a single response. 2PEF can separate inorganic from organic samples, but the fact that KS always contain some amount of fluorescent material limits the efficiency of this parameter alone. A way to increase discriminative power may be to add a spectral dimension, but it is still not completely unambiguous. Remarkably, SHG—more precisely SHG/THG probability—allows a clearer separation between the KS types tested in this study. Finally, a combined SHG/pTHG criterion provides an efficient and unambiguous way to classify all of the KS fragments studied. We also used pTHG imaging to probe the internal structure of KS fragments. It showed the radial crystalline orientation of concentric subdomains in carbonate apatite microparticles without the need for electron microscopy. pTHG images also produced different patterns in COM and COD fragments, indicating that COM fragments are mainly birefringent monocrystals, whereas COD fragments are composed of microdomains with different crystalline orientations. All of these observations suggest the potential for developing new diagnostic tools based on multimodal multiphoton metrics of KS fragments. Such development would first require further populating the parametric plot to determine the limits of multiphoton-based classification. From a practical point of view, the ongoing advances in compact multimodal multiphoton microscopes suitable for clinical use[48] and the simple sample preparation scheme shown here indicate that there is scope to optimize a multiphoton classification scheme in a high-throughput clinical setting.

ASSOCIATED CONTENT

Supporting Information

The Supporting Information is available free of charge at https://pubs.acs.org/doi/10.1021/acsphotonics.3c00651.

Table of the chemical composition, crystalline structure, protein content, and number of fragments analyzed; full theoretical analysis of polarization-resolved third-harmonic generation with diagrams of the relevant geometries of beam interaction with the material; 2PEF emitted in a red wavelength range excited at 950 nm; and photographs of cystine A and cystine B (PDF)

AUTHOR INFORMATION

Corresponding Authors

Matthew Gleeson − *Laboratory for Optics and Biosciences, École Polytechnique, CNRS, Inserm, Institut Polytechnique de Paris, 91128 Palaiseau, France;* orcid.org/0009-0009-0551-1153; Email: matthew.gleeson@polytechnique.edu

Marie-Claire Schanne-Klein − *Laboratory for Optics and Biosciences, École Polytechnique, CNRS, Inserm, Institut*

Polytechnique de Paris, 91128 Palaiseau, France; orcid.org/0000-0003-3026-8932; Email: marie-claire.schanne-klein@polytechnique.edu

Emmanuel Beaurepaire − *Laboratory for Optics and Biosciences, École Polytechnique, CNRS, Inserm, Institut Polytechnique de Paris, 91128 Palaiseau, France;* orcid.org/0000-0002-2082-8214; Email: emmanuel.beaurepaire@polytechnique.edu

Authors

Joséphine Morizet − *Laboratory for Optics and Biosciences, École Polytechnique, CNRS, Inserm, Institut Polytechnique de Paris, 91128 Palaiseau, France*

Pierre Mahou − *Laboratory for Optics and Biosciences, École Polytechnique, CNRS, Inserm, Institut Polytechnique de Paris, 91128 Palaiseau, France;* orcid.org/0000-0003-4452-1011

Michel Daudon − *AP HP, Département de Physiologie, Hôpital Tenon, Paris 75970, France*

Dominique Bazin − *CNRS, Institut de Chimie Physique, Université Paris-Saclay, 91405 Orsay, France*

Chiara Stringari − *Laboratory for Optics and Biosciences, École Polytechnique, CNRS, Inserm, Institut Polytechnique de Paris, 91128 Palaiseau, France;* orcid.org/0000-0002-0550-7463

Complete contact information is available at: https://pubs.acs.org/10.1021/acsphotonics.3c00651

Author Contributions

[‖]M.G., J.M., M.-C.S.-K., and E.B. contributed equally to this work. D.B., M.-C.S.-K., and E.B. designed the study. J.M., P.M., C.S., and E.B. optimized the microscopy setup. M.G. and J.M. performed the experiments and analyzed the data. M.D. and D.B. provided human samples and biomedical interpretation. J.M., E.B., and M.-C.S.-K. developed the pTHG theoretical analysis. M.G., M.-C.S.-K., and E.B. wrote the manuscript with input from all other authors.

Funding

Agence Nationale de la Recherche (ANR-EQPX-0029, ANR-10-INBS-04, and ANR-15-CE11-0012) and Fondation Bettencourt-Schueller (Brain Harmonics).

Notes

The authors declare no competing financial interest.

■ ACKNOWLEDGMENTS

The authors thank all members of the advanced microscopies group at the Laboratory for Optics and Biosciences for discussions on biomicroscopy. The authors also thank Max Zimmerley and Nicolas Olivier for discussions on polarized THG microscopy and Christine V. Putnis from the University of Münster for providing the ACO sample.

■ REFERENCES

(1) Daudon, M.; Bazin, D.; André, G.; Jungers, P.; Cousson, A.; Chevallier, P.; Véron, E.; Matzen, G. Examination of whewellite kidney stones by scanning electron microscopy and powder neutron diffraction techniques. *J. Appl. Crystallogr.* **2009**, *42*, 109−115.

(2) Romero, V.; Akpinar, H.; Assimos, D. G. Kidney stones: a global picture of prevalence, incidence, and associated risk factors. *Rev. Urol.* **2010**, *12*, e86−e96.

(3) Millan, A. Crystal Growth Shape of Whewellite Polymorphs: Influence of Structure Distortions on Crystal Shape. *Cryst. Growth Des.* **2001**, *1*, 245−254.

(4) Ryall, R. L.; Chauvet, M. C.; Grover, P. K. Intracrystalline proteins and urolithiasis: a comparison of the protein content and ultrastructure of urinary calcium oxalate monohydrate and dihydrate crystals. *BJU Int.* **2005**, *96*, 654−663.

(5) Grover, P. K.; Thurgood, L. A.; Fleming, D. E.; Bronswijk, Wv.; Wang, T.; Ryall, R. L. Intracrystalline urinary proteins facilitate degradation and dissolution of calcium oxalate crystals in cultured renal cells. *Am. J. Physiol.: Renal, Physiol.* **2008**, *294*, F355−F361.

(6) Cloutier, J.; Villa, L.; Traxer, O.; Daudon, M. Kidney stone analysis: "Give me your stone, I will tell you who you are!". *World J. Urol.* **2015**, *33*, 157−169.

(7) Güler, A.; Erbin, A.; Ucpinar, B.; Savun, M.; Sarilar, O.; Akbulut, M. F. Comparison of miniaturized percutaneous nephrolithotomy and standard percutaneous nephrolithotomy for the treatment of large kidney stones: a randomized prospective study. *Urolithiasis* **2019**, *47*, 289−295.

(8) Deem, S.; DeFade, B.; Modak, A.; Emmett, M.; Martinez, F.; Davalos, J. Percutaneous Nephrolithotomy Versus Extracorporeal Shock Wave Lithotripsy for Moderate Sized Kidney Stones. *Urology* **2011**, *78*, 739−743.

(9) Keat, W. O. L.; Somani, B.; Pietropaolo, A.; Chew, B.; Chai, C.; Inoue, T.; Ragoori, D.; Biligere, S.; Galosi, A.; Pavia, M.; Milanese, G.; Ahn, T.; More, S.; Sarica, K.; Traxer, O.; Teoh, J.; Gauhar, V.; Castellani, D. Do Hounsfield Units have any significance in predicting intra- and postoperative outcomes in retrograde intrarenal surgery using Holmium and Thulium fiber laser? Results from the FLEXible ureteroscopy Outcomes Registry (FLEXOR). *World J. Urol.* **2023**, DOI: 10.1007/s00345-023-04362-7.

(10) Primiano, A.; Persichilli, S.; Ferraro, P. M.; Minucci, A.; Gambaro, G.; Urbani, A.; Gervasoni, J. A combination of infrared spectroscopy and morphological analysis allows successfully identifying rare crystals and atypical urinary stones. *Ann. Ist. Super. Sanita* **2019**, *55*, 205−208.

(11) Chang, C.-C.; Chiu, Y. Applying quantitative micro-Raman spectroscopy to analyze stone compositions extracted from ureteroscopic lithotripsy urine. *Urol. Sci.* **2017**, *28*, 19−22.

(12) Cui, X.; Zhao, Z.; Zhang, G.; Chen, S.; Zhao, Y.; Lu, J. Analysis and classification of kidney stones based on Raman spectroscopy. *Biomed. Opt. Express* **2018**, *9*, 4175−4183.

(13) Castiglione, V.; Sacré, P.-Y.; Cavalier, E.; Hubert, P.; Gadisseur, R.; Ziemons, E. Raman chemical imaging, a new tool in kidney stone structure analysis: Case-study and comparison to Fourier Transform Infrared spectroscopy. *PLoS One* **2018**, *13*, e0201460.

(14) Zhu, W.; Sun, Z.; Ye, L.; Zhang, X.; Xing, Y.; Zhu, Q.; Yang, F.; Jiang, G.; Chen, Z.; Chen, K.; En, M.; Wang, L. Preliminary assessment of a portable Raman spectroscopy system for postoperative urinary stone analysis. *World J. Urol.* **2022**, *40*, 229−235.

(15) Costa-Bauzá, A.; Grases, F.; Julià, F. The power of desktop scanning electron microscopy with elemental analysis for analyzing urinary stones. *Urolithiasis* **2023**, *51*, No. 50.

(16) Greasley, J.; Goolcharan, S.; Andrews, R. Quantitative phase analysis and microstructural characterization of urinary tract calculi with X-ray diffraction Rietveld analysis on a Caribbean island. *J. Appl. Crystallogr.* **2022**, *55*, 46−57.

(17) Zhang, X.; Ma, J.; Wang, N.; Lin, C. Urinary stone composition analysis of 3684 patients in the eastern Shandong region of China. *J. Int. Med. Res.* **2019**, *48*, No. 030006051988726.

(18) Siener, R.; Herwig, H.; Rüdy, J.; Schaefer, R.; Lossin, P.; Hesse, A. Urinary stone composition in Germany: results from 45,783 stone analyses. *World Journal of Urology* **2022**, *40*, 1813−1820.

(19) Mijangos, F.; Celaya, M. A.; Gainza, F. J.; Imaz, A.; Arana, E. SEM−EDX linear scanning: a new tool for morpho-compositional analysis of growth bands in urinary stones. *JBIC J. Biol. Inorg. Chem.* **2020**, *25*, 705−715.

(20) Daudon, M.; Dessombz, A.; Frochot, V.; Letavernier, E.; Haymann, J.-P.; Jungers, P.; Bazin, D. Comprehensive morpho-constitutional analysis of urinary stones improves etiological diagnosis and therapeutic strategy of nephrolithiasis. *C. R. Chim.* **2016**, *19*, 1470−1491.

(21) Winfree, S.; Weiler, C.; Bledsoe, S. B.; Gardner, T.; Sommer, A. J.; Evan, A. P.; Lingeman, J. E.; Krambeck, A. E.; Worcester, E. M.; El-Achkar, T. M.; Williams, J. C. Multimodal imaging reveals a unique autofluorescence signature of Randall's plaque. *Urolithiasis* **2021**, *49*, 123−135.
(22) Pucetaite, M.; Tamosaityte, S.; Engdahl, A.; Ceponkus, J.; Sablinskas, V.; Uvdal, P. Microspectroscopic infrared specular reflection chemical imaging of multi-component urinary stones: MIR vs. FIR. *Cent. Eur. J. Chem.* **2014**, *12*, 44−52.
(23) Pucetaite, M.; Tamosaityte, S.; Galli, R.; Sablinskas, V.; Steiner, G. Microstructure of urinary stones as studied by means of multimodal nonlinear optical imaging. *J. Raman Spectrosc.* **2017**, *48*, 22−29.
(24) Morizet, J.; Ducourthial, G.; Supatto, W.; Boutillon, A.; Legouis, R.; Schanne-Klein, M.-C.; Stringari, C.; Beaurepaire, E. High-speed polarization-resolved third-harmonic microscopy. *Optica* **2019**, *6*, 385−388.
(25) Zhang, J.; Wang, L.; Zhang, W.; Putnis, C. V. Role of Hyperoxaluria/Hypercalciuria in Controlling the Hydrate Phase Selection of Pathological Calcium Oxalate Mineralization. *Cryst. Growth Des.* **2021**, *21*, 683−691.
(26) Bhatta, K. M.; Prien, E. L., Jr.; Dretler, S. P. Cystine calculi–rough and smooth: a new clinical distinction. *J. Urol.* **1989**, *142*, 937−940.
(27) Boyd, R. W. *Nonlinear Optics*; Academic Press, 2020 DOI: 10.1016/C2015-0-05510-1.
(28) Barad, Y.; Eisenberg, H.; Horowitz, M.; Silberberg, Y. Nonlinear scanning laser microscopy by third harmonic generation. *Appl. Phys. Lett.* **1997**, *70*, 922−924.
(29) Cheng, J.-X.; Xie, X. S. Green's function formulation for third-harmonic generation microscopy. *J. Opt. Soc. Am. B* **2002**, *19*, 1604−1610.
(30) Oron, D.; Tal, E.; Silberberg, Y. Depth-resolved multiphoton polarization microscopy by third-harmonic generation. *Opt. Lett.* **2003**, *28*, 2315−2317.
(31) Kosugi, J.-i.; Kajikawa, K. Phase-matched third-harmonic generation from nematic liquid crystals. *Appl. Phys. Lett.* **2004**, *84*, 5013−5015.
(32) Pillai, R. S.; Oh-e, M.; Yokoyama, H.; Brakenhoff, G. J.; Müller, M. Imaging colloidal particle induced topological defects in a nematic liquid crystal using third harmonic generation microscopy. *Opt. Express* **2006**, *14*, 12976−12983.
(33) Zimmerley, M.; Mahou, P.; Débarre, D.; Schanne-Klein, M.-C.; Beaurepaire, E. Probing Ordered Lipid Assemblies with Polarized Third-Harmonic-Generation Microscopy. *Phys. Rev. X* **2013**, *3*, No. 011002.
(34) Morizet, J.; Sartorello, G.; Dray, N.; Stringari, C.; Beaurepaire, E.; Olivier, N. Modeling nonlinear microscopy near index-mismatched interfaces. *Optica* **2021**, *8*, 944−951.
(35) Morizet, J.; Olivier, N.; Mahou, P.; Boutillon, A.; Stringari, C.; Beaurepaire, E. Third harmonic imaging contrast from tubular structures in the presence of index discontinuity. *Sci. Rep.* **2023**, *13*, No. 7850.
(36) Pras, E.; Arber, N.; Aksentijevich, I.; Katz, G.; Schapiro, J. M.; Prosen, L.; Gruberg, L.; Harel, D.; Liberman, U.; Weissenbach, J.; Pras, M.; Kastner, D. L. Localization of a gene causing cystinuria to chromosome 2p. *Nat. Genet.* **1994**, *6*, 415−419.
(37) Calonge, M. J.; Gasparini, P.; Chillarón, J.; Chillón, M.; Gallucci, M.; Rousaud, F.; Zelante, L.; Testar, X.; Dallapiccola, B.; Di Silverio, F.; Barceló, P.; Estivill, X.; Zorzano, A.; Nunes, V.; Palacín, M. Cystinuria caused by mutations in rBAT, a gene involved in the transport of cystine. *Nat. Genet.* **1994**, *6*, 420−425.
(38) Bazin, D.; Daudon, M.; André, G.; Weil, R.; Véron, E.; Matzen, G. Therapy modifies cystine kidney stones at the macroscopic scale. Do such alterations exist at the mesoscopic and nanometre scale? *J. Appl. Crystallogr.* **2014**, *47*, 719−725.
(39) Crutcher, R.; Crutcher, H. Calcium oxalate phytoliths in environmental samples. *Microscope* **2019**, *67*, 3−11.
(40) Lussier, F.; Thibault, V.; Charron, B.; Wallace, G. Q.; Masson, J.-F. Deep learning and artificial intelligence methods for Raman and surface-enhanced Raman scattering. *TrAC, Trends Anal. Chem.* **2020**, *124*, No. 115796.
(41) Mathurin, J.; Deniset-Besseau, A.; Bazin, D.; Dartois, E.; Wagner, M.; Dazzi, A. Photothermal AFM-IR spectroscopy and imaging: Status, challenges, and trends. *J. Appl. Phys.* **2022**, *131*, No. 010901.
(42) Carpentier, X.; Daudon, M.; Traxer, O.; Jungers, P.; Mazouyes, A.; Matzen, G.; Véron, E.; Bazin, D. Relationships Between Carbonation Rate of Carbapatite and Morphologic Characteristics of Calcium Phosphate Stones and Etiology. *Urology* **2009**, *73*, 968−975.
(43) Colboc, H.; Moguelet, P.; Letavernier, E.; Frochot, V.; Bernaudin, J.-f.; Weil, R.; Rouzière, S.; Senet, P.; Bachmeyer, C.; Laporte, N.; Lucas, I.; Descamps, V.; Amode, R.; Brunet-Possenti, F.; Kluger, N.; Deschamps, L.; Dubois, A.; Reguer, S.; Somogyi, A.; Bazin, D.; et al. Pathologies related to abnormal deposits in dermatology: a physico-chemical approach. *C. R. Chim.* **2022**, *25*, 1−32.
(44) Ben Lakhdar, A.; Daudon, M.; Mathieu, M.-C.; Kellum, A.; Balleyguier, C.; Bazin, D. Underlining the complexity of the structural and chemical characteristics of ectopic calcifications in breast tissues through FE-SEM and μFTIR spectroscopy. *C. R. Chim.* **2016**, *19*, 1610−1624.
(45) Bazin, D.; André, G.; Weil, R.; Matzen, G.; Emmanuel, V.; Carpentier, X.; Daudon, M. Absence of Bacterial Imprints on Struvite-containing Kidney Stones: A Structural Investigation at the Mesoscopic and Atomic Scale. *Urology* **2012**, *79*, 786−790.
(46) Pradhan, P.; Guo, S.; Ryabchykov, O.; Popp, J.; Bocklitz, T. W. Deep learning a boon for biophotonics? *J. Biophotonics* **2020**, *13*, No. e201960186.
(47) Blokker, M.; Hamer, P. C. d. W.; Wesseling, P.; Groot, M. L.; Veta, M. Fast intraoperative histology-based diagnosis of gliomas with third harmonic generation microscopy and deep learning. *Sci. Rep.* **2022**, *12*, No. 11334.
(48) Cheng, Q.-d.; Chung, H.-Y.; Schubert, R.; Chia, S.-H.; Falke, S.; Mudogo, C. N.; Kärtner, F. X.; Chang, G.; Betzel, C. Protein-crystal detection with a compact multimodal multiphoton microscope. *Commun. Biol.* **2020**, *3*, No. 569.

https://doi.org/10.1021/acsphotonics.3c00651
ACS Photonics 2023, 10, 3594−3604

Supporting Information

Kidney stone classification using multimodal multiphoton microscopy

Matthew Gleeson[a]†*, Joséphine Morizet[a]†, Pierre Mahou[a], Michel Daudon[b], Dominique Bazin[c], Chiara Stringari[a], Marie-Claire Schanne-Klein[a]‡*, Emmanuel Beaurepaire[a]‡*

[a] Laboratory for Optics and Biosciences, École Polytechnique, CNRS, Inserm, Institut Polytechnique de Paris, 91120, Palaiseau, France

[b] Hôpital Tenon, AP HP, Département de Physiologie, Paris, France

[c] Université Paris-Saclay, CNRS, Institut de Chimie Physique, 91405, Orsay, France

Corresponding Authors:
*Email: matthew.gleeson@polytechnique.edu
*Email: marie-claire.schanne-klein@polytechnique.edu
*Email: emmanuel.beaurepaire@polytechnique.edu

† M.G and J.M contributed equally to this paper; ‡ M-C.S-K and E.B contributed equally to this paper.

Supporting Information includes 7 pages, 1 table and 3 figures:

S1. Table describing chemical composition, crystalline structure, protein content, number of fragments for 2PEF/SHG and prTHG in pTHG analysis

Sample	Chemical composition	Crystalline structure	Protein content	Number of fragments - THG/SHG/2PEF	Number of fragments - pTHG
ACO	Calcium Oxalate CaC_2O_4	Amorphous Centrosymmetric	0 %	182	50
COM A	Calcium Oxalate Monohydrate CaC_2O_4 H_2O (Whewellite)	Monoclinic: $P2_1/c$ Centrosymmetric	Non zero	381	50
COM B	Calcium Oxalate Monohydrate CaC_2O_4 H_2O (Whewellite)	Monoclinic: $P2_1/c$ Centrosymmetric	Non zero	519	50
COD 99% A	Calcium Oxalate Dihydrate $CaC_2O_4 2H_2O$ (Weddelite)	Tetragonal: I4/m Centrosymmetric	1 %	807	50
COD 99% B	Calcium Oxalate Dihydrate $CaC_2O_4 2H_2O$ (Weddelite)	Tetragonal: I4/m Centrosymmetric	1 %	711	50
COD 96%	Calcium Oxalate Dihydrate $CaC_2O_4 2H_2O$ (Weddelite)	Tetragonal: I4/m Centrosymmetric	4 %	783	50
Cyst. A	Cystine $(SCH_2CH(NH_2)CO_2H)_2$	Hexagonal: $P6_122$ Non-centrosymmetric	1-3 %	1217	50
Cyst. B	Cystine $(SCH_2CH(NH_2)CO_2H)_2$	Hexagonal: $P6_122$ Non-centrosymmetric	1-3 %	2061	50
Carb. Apt.	Carbonate apatite $Ca_{9.75}[(PO_4)_{5.5}(CO_3)_{0.5}]CO_3$	Hexagonal: $\overline{P6}$ Non-centrosymmetric	4 %	1054	50

Table S1: Samples under study. All samples are kidney stones from Tenon hospital (Paris, France) except for ACO that is a synthetic amorphous calcium oxalate provided by University of Münster[(1)] (Germany).

S2. P-THG theoretical analysis

We derive here the polarization resolved THG signal from anisotropic materials in focussed beam condition. Let's write the fundamental ($n = 1$) and THG ($n = 3$) electric fields in the paraxial approximation:

$$\vec{E}^{(n)}(\vec{r},t) = \vec{E}^{(n)}(\vec{r})\, e^{-in\omega t} + cc = \vec{A}^{(n)}(\vec{r})\, e^{i(k_n z - n\omega t)} + cc, \quad (1a)$$

where $\vec{A}^{(n)}(\vec{r})$ is a Gaussian beam characterized by a confocal parameter b:

$$\vec{A}^{(n)}(\vec{r}) = \frac{\vec{\mathcal{A}}_n}{1+i\zeta}\, e^{-r^2/w_{n,0}^2(1+i\zeta)}, \tag{1b}$$

with $\zeta = 2z/b$ and $w_{n,0}^2 = b/k_n$.

The THG response is described by a third-order nonlinear susceptibility tensor $\chi^{(3)}$ that induces a nonlinear polarization $\vec{P}^{(3)}(\vec{r},t)$ at the third harmonic frequency 3ω as follows:

$$P_i^{(3)}(\vec{r}) = \epsilon_0 \sum_{j,k,l} \chi_{ijkl}^{(3)}\, E_j(\vec{r}) E_k(\vec{r}) E_l(\vec{r}) \tag{2}$$

Here i,j,k,l refer to the Cartesian components of the fields and we have dropped the exponent (1) for the fundamental field. The third-order susceptibility tensor $\chi^{(3)}$ for THG has 21 independent components when the Kleinman symmetry applies. To further simplify the analysis and get tractable expressions, we consider a material with hexagonal symmetry as in previous studies[(2), (3), (4)] which reduces the number of nonzero components to 21, with only 3 independent values[(5)]. Considering that the crystal main axis is x, we get:

$$\chi_{\parallel}^{(3)} = \chi_{xxxx}^{(3)} \tag{3a}$$

$$\chi_{\perp}^{(3)} = \chi_{yyyy}^{(3)} = \chi_{zzzz}^{(3)} = 3\,\chi_{yyzz}^{(3)} = 3\,\chi_{yzzy}^{(3)} = 3\,\chi_{yzyz}^{(3)} = 3\,\chi_{zzyy}^{(3)} = 3\,\chi_{zyyz}^{(3)} = 3\,\chi_{zyzy}^{(3)} \tag{3b}$$

$$\chi_{cr}^{(3)} = 3\,\chi_{xxyy}^{(3)} = 3\,\chi_{xyxy}^{(3)} = 3\,\chi_{xyyx}^{(3)} = 3\,\chi_{yyxx}^{(3)} = 3\,\chi_{yxyx}^{(3)} = 3\,\chi_{yxxy}^{(3)} = 3\,\chi_{xxzz}^{(3)} = 3\,\chi_{xzxz}^{(3)} = 3\,\chi_{xzzx}^{(3)} = 3\,\chi_{zzxx}^{(3)} = 3\,\chi_{zxzx}^{(3)} = 3\,\chi_{zxxz}^{(3)} \tag{3c}$$

Considering that the crystal axis x lies within the imaging plane XY, at angle θ_0 to the axis X, and neglecting the electric field component along the microscope axis Z, aligned with the crystal axis z ($Z = z$), equation (2) simplifies to:

$$\vec{P}^{(3)}(\vec{r}) = \epsilon_0 \begin{pmatrix} E_x\left(\chi_{\parallel}^{(3)} E_x^2 + \chi_{cr}^{(3)} E_y^2\right) \\ E_y\left(\chi_{cr}^{(3)} E_x^2 + \chi_{\perp}^{(3)} E_y^2\right) \\ 0 \end{pmatrix}_{(x,y,z)} \tag{4}$$

For a linear incident polarization at angle ϕ to the axis X, $E_x(\vec{r}) = A^{(1)}(\vec{r})\cos\left(\phi - \phi_0\right) e^{ik_e z}$ and $E_y(\vec{r}) = A^{(1)}(\vec{r})\sin\left(\phi - \phi_0\right) e^{ik_o z}$, where k_e and k_o are the extraordinary (propagation along the axis x) and ordinary (propagation $\perp$ x) wave vectors.

This nonlinear polarization acts as a nonlinear source term in the wave propagation equation at 3ω. Using the Gaussian beam expressions (1b) of the fundamental and THG beams and following a similar approach as in[5], one get for a material between z_a and z_b planes:

$$\mathcal{A}_{3,x}(\phi) = \frac{3i\omega}{2n_{3e}c}\begin{bmatrix} \chi_{\parallel}^{(3)} cos^3(\phi-\phi_0)\, J(\Delta k_{eeee}, z_a, z_b) \\ +\chi_{cr}^{(3)} \cos(\phi-\phi_0)\, sin^2(\phi-\phi_0)\, J(\Delta k_{eooe}, z_a, z_b) \end{bmatrix} \mathcal{A}_1^3 \quad (5a)$$

$$\mathcal{A}_{3,y}(\phi) = \frac{3i\omega}{2n_{3e}c}\begin{bmatrix} \chi_{cr}^{(3)} cos^2(\phi-\phi_0) \sin(\phi-\phi_0)\, J(\Delta k_{oeeo}, z_a, z_b) \\ +\chi_{\perp}^{(3)} sin^3(\phi-\phi_0)\, J(\Delta k_{oooo}, z_a, z_b) \end{bmatrix} \mathcal{A}_1^3 \quad (5b)$$

$$\mathcal{A}_{3,z}(\phi) = 0 \quad (5c)$$

$$\text{With } J(\Delta k, z_a, z_b) = \int_{z_a}^{z_b} \frac{e^{i\Delta k z'}\, dz'}{(1+2iz'/b)^2} \quad (6)$$

(i) Considering a bulk material with normal dispersion, the phase mismatch $\Delta k_{uvwx} = k_u^{(3)} - k_v^{(1)} - k_w^{(1)} - k_x^{(1)}$ $(u,v,w,x = o,e)$ is negative and the integral $J(\Delta k_{uvwx}, z_a, z_b)$ vanishes for all cases, except Δk_{oeeo} for positive birefringence or Δk_{eooe} for negative birefringence[2, 3, 4]. As a result, the THG intensity writes:

$$THG_{biref}(\phi) \propto cos^4(\phi-\phi_0) sin^2(\phi-\phi_0) \left|\chi_{cr}^{(3)}\right|^2 I^3 \text{ for positive birefringence} \quad (7a)$$

$$THG_{biref}(\phi) \propto cos^2(\phi-\phi_0) sin^4(\phi-\phi_0) \left|\chi_{cr}^{(3)}\right|^2 I^3 \text{ for negative birefringence} \quad (7b)$$

Here *I* is the intensity of the incident beam at ω. This calculation also shows that THG vanishes in isotropic bulk materials with normal dispersion[5, 6].

(ii) Let us consider now that the beam is focused at the surface of the anisotropic material under study, *i.e.* an interface perpendicular to the beam propagation direction. This situation can be modelled as the interface between an anisotropic material (characterized by $\chi_{material}^{(3)} - \chi_{surroundings}^{(3)}$) and vacuum[7]. All the integrals *J* must be calculated for $z_a = 0$ and have similar nonzero values. Neglecting polarization-dependent field distortions, the pTHG response can thus be written in the general form:

$$THG_H(\phi) \propto \begin{pmatrix} \left|\chi_{\parallel}^{(3)} cos^3(\phi-\phi_0) + \chi_{cr}^{(3)} cos(\phi-\phi_0) sin^2(\phi-\phi_0)\right|^2 \\ +\left|\chi_{\parallel}^{(3)} cos^2(\phi-\phi_0) sin(\phi-\phi_0) + \chi_{\perp}^{(3)} sin^3(\phi-\phi_0)\right|^2 \end{pmatrix} I^3 \quad (8)$$

This response can exhibit various profiles depending on the ratios between the three independent $\chi^{(3)}$ tensor elements (see main text).

(iii) In the case of pTHG from a vertical interface, *i.e.* when a linearly polarized excitation beam is focused near a vertical discontinuity of the refractive index, the THG process is significantly altered by field distortions[(8), (9)] and cannot be easily described analytically. In high-NA microscopy experiments, the signal is often found to follow a polarization dependence in the form[(9), (10)]:

$$THG_V(\phi) \propto A + Bcos^2(\phi - \phi_0)I^3 \quad (9)$$

where A and B are constants.

S3. Geometry and notations for pTHG theory.

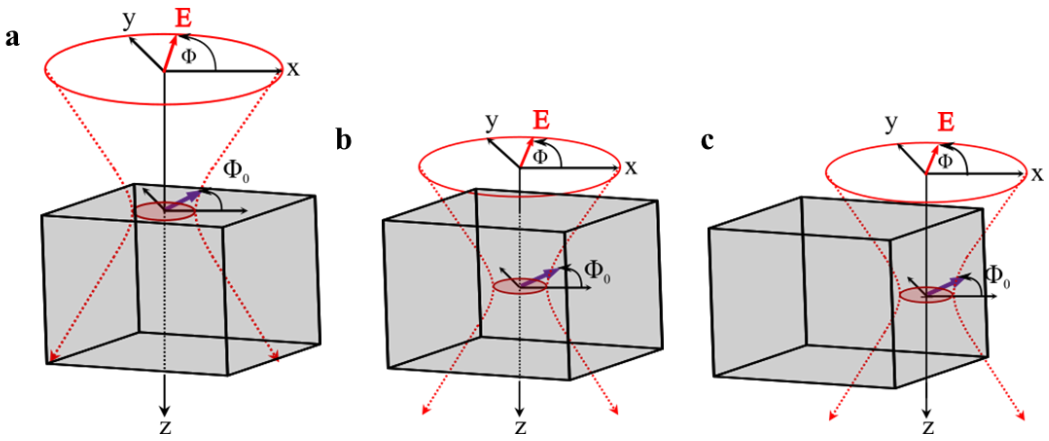

Figure S1. Geometry and notations for pTHG theory. a THG from the surface of an anisotropic medium, case (i) in main text **b** THG from the bulk of a homogeneous material, case (ii) in main text **c** THG from a flat vertical interface parallel to the beam propagation, case (iii) in main text. Φ refers to angle on excitation laser polarization shown as the red arrow, Φ_0 refers to the axis of the material, which in this cartoon is parallel to the crystal edge, its direction is shown by the purple arrow. Both Φ and Φ_0 are in the xy plane.

S4. 2PEF red channel response for excitation at 950 nm samples

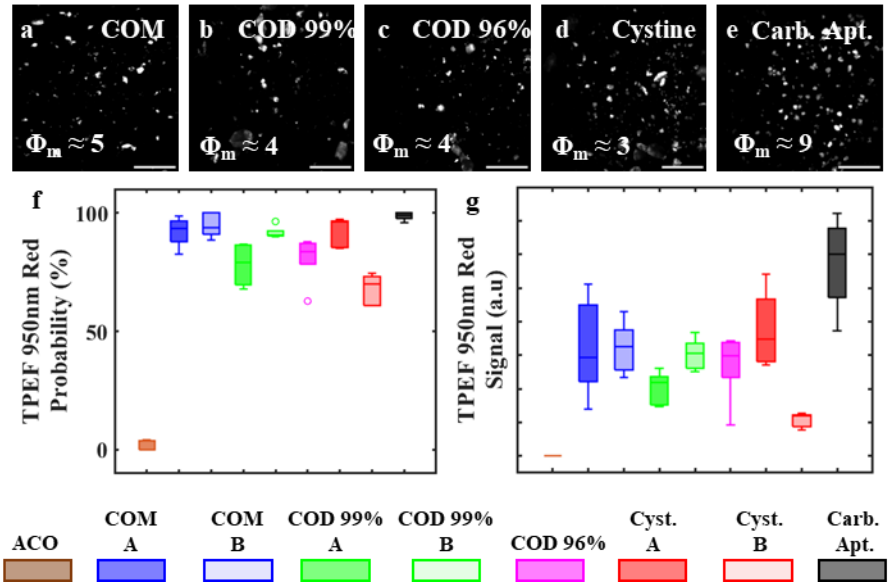

Figure S2. 2PEF red channel response upon excitation at 950 nm of several kidney stones and reference samples. a COM **b** COD 99% **c** COD 96% **d** Cystine and **e** Carbonate apatite samples. Image contrast has been stretched for the sake of clarity. Scale bars are 200 µm. Inset Φ_m is mean photon count for averaged sample type. Box plots for 2PEF **f** probability and **g** signal.

S5. Photographs of Cystine samples

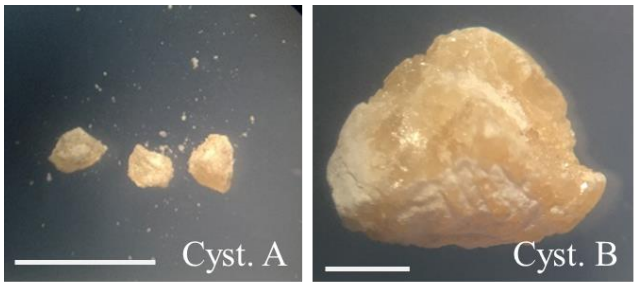

Figure S3. Two different cystine crystals. Scale bars are 2 mm.

Supplementary References:

1. Zhang, J.; Wang, L.; Zhang, W.; Putnis, C. V., Role of Hyperoxaluria/Hypercalciuria in Controlling the Hydrate Phase Selection of Pathological Calcium Oxalate Mineralization. *Crystal Growth & Design* **2021,** *21* (1), 683-691.
2. Kosugi, J.-i.; Kajikawa, K., Phase-matched third-harmonic generation from nematic liquid crystals. *Applied Physics Letters* **2004,** *84*, 5013-5015.
3. Pillai, R. S.; Oh-e, M.; Yokoyama, H.; Brakenhoff, G. J.; Müller, M., Imaging colloidal particle induced topological defects in a nematic liquid crystal using third harmonic generation microscopy. *Opt. Express* **2006,** *14* (26), 12976-12983.
4. Morizet, J.; Ducourthial, G.; Supatto, W.; Boutillon, A.; Legouis, R.; Schanne-Klein, M.-C.; Stringari, C.; Beaurepaire, E., High-speed polarization-resolved third-harmonic microscopy. *Optica* **2019,** *6* (3), 385-388.
5. Boyd, R. W., *Nonlinear optics*. Academic press: 2020, https://doi.org/10.1016/C2015-0-05510-1.
6. Oron, D.; Tal, E.; Silberberg, Y., Depth-resolved multiphoton polarization microscopy by third-harmonic generation. *Opt. Lett.* **2003,** *28* (23), 2315-2317.
7. Olivier, N.; Beaurepaire, E., Third-harmonic generation microscopy with focus-engineered beams: a numerical study. *Optics Express* **2008,** *16* (19), 14703-14715.
8. Morizet, J.; Sartorello, G.; Dray, N.; Stringari, C.; Beaurepaire, E.; Olivier, N., Modeling nonlinear microscopy near index-mismatched interfaces. *Optica* **2021,** *8* (7), 944-951.
9. Morizet, J.; Olivier, N.; Mahou, P.; Boutillon, A.; Stringari, C.; Beaurepaire, E., Third harmonic imaging contrast from tubular structures in the presence of index discontinuity. *Scientific Reports* **2023,** *13* (1), 7850, https://doi.org/10.1038/s41598-023-34528-7.
10. Zimmerley, M.; Mahou, P.; Débarre, D.; Schanne-Klein, M.-C.; Beaurepaire, E., Probing Ordered Lipid Assemblies with Polarized Third-Harmonic-Generation Microscopy. *Physical Review X* **2013,** *3* (1), 011002, https://doi.org/10.1103/PhysRevX.3.011002.